Tashiro et al. *NPG Asia Materials* (2024)16:55
https://doi.org/10.1038/s41427-024-00574-4

NPG Asia Materials

ARTICLE Open Access

Metasurface-enabled multifunctional single-frequency sensors without external power

Masaya Tashiro[1], Kosuke Ide[1], Kosei Asano[1], Satoshi Ishii[2,3,4], Yuta Sugiura[2,5], Akira Uchiyama[2,6] and Hiroki Wakatsuchi[1,2]

Abstract

IoT sensors are crucial for visualizing multidimensional and multimodal information and enabling future IT applications/services such as cyber-physical spaces, digital twins, autonomous driving, smart cities and virtual/augmented reality (VR or AR). However, IoT sensors need to be battery-free to realistically manage and maintain the growing number of available sensing devices. Here, we provide a novel sensor design approach that employs metasurfaces to enable multifunctional sensing without requiring an external power source. Importantly, unlike existing metasurface-based sensors, our metasurfaces can sense multiple physical parameters even at a fixed frequency by breaking classic harmonic oscillations in the time domain, making the proposed sensors viable for usage with limited frequency resources. Moreover, we provide a method for predicting physical parameters via the machine learning-based approach of random forest regression. The sensing performance was confirmed by estimating the temperature and light intensity, and excellent determination coefficients larger than 0.96 were achieved. Our study affords new opportunities for sensing multiple physical properties without relying on an external power source or requiring multiple frequencies, which markedly simplifies and facilitates the design of next-generation wireless communication systems.

Introduction

The ability to perceive and interpret information from several dimensions and modes is essential for advancing future information technologies[1–3]. Currently, various sensors are used to detect diverse physical parameters, including temperature, light intensity, humidity, pressure, sound, angle, posture, pollution and radiation, as shown in Fig. 1a[4]. These sensors serve numerous purposes, such as optimizing power consumption, enhancing health care, preserving the environment, supporting agriculture and ensuring security. Recently, they have been incorporated into wireless networks such as Internet of Things (IoT) systems, which enable future cyber-physical spaces, digital twins, autonomous driving, smart cities and virtual/augmented reality (VR or AR)[1,2,5]. This trend is reflected in the global prevalence of IoT devices, specifically the substantial rapid annual growth rate of two billion or more devices per year. Nevertheless, the growing demand for IoT sensors has raised notable concerns about managing numerous devices with limited human resources. More precisely, although these devices rely on batteries to establish communication with remote systems, it is not feasible to manually provide a new battery for every individual device. Therefore, battery-free or maintenance-free sensors are ideal for next-generation IoT systems.

Metasurfaces can serve as a viable option in this scenario for detecting physical quantities without needing battery replacement[6–10]. Metasurfaces are artificially engineered structures that exhibit distinct behavior on the basis of the properties of their subwavelength unit cells and the spectra of the incoming wave[11–13]. Metasurfaces exhibit a robust response to an incoming wave at a designed resonant frequency and can efficiently sense physical properties such as light intensity and temperature by incorporating vanadium dioxide, MEMS, thermistors and/or photocells (i.e., photoresistors) into the

---

Correspondence: Hiroki Wakatsuchi (wakatsuchi.hiroki@nitech.ac.jp)
[1]Department of Engineering, Nagoya Institute of Technology, Nagoya, Aichi 466-8555, Japan
[2]Precursory Research for Embryonic Science and Technology (PRESTO), Japan Science and Technology Agency (JST), Kawaguchi, Saitama 332-0012, Japan
Full list of author information is available at the end of the article

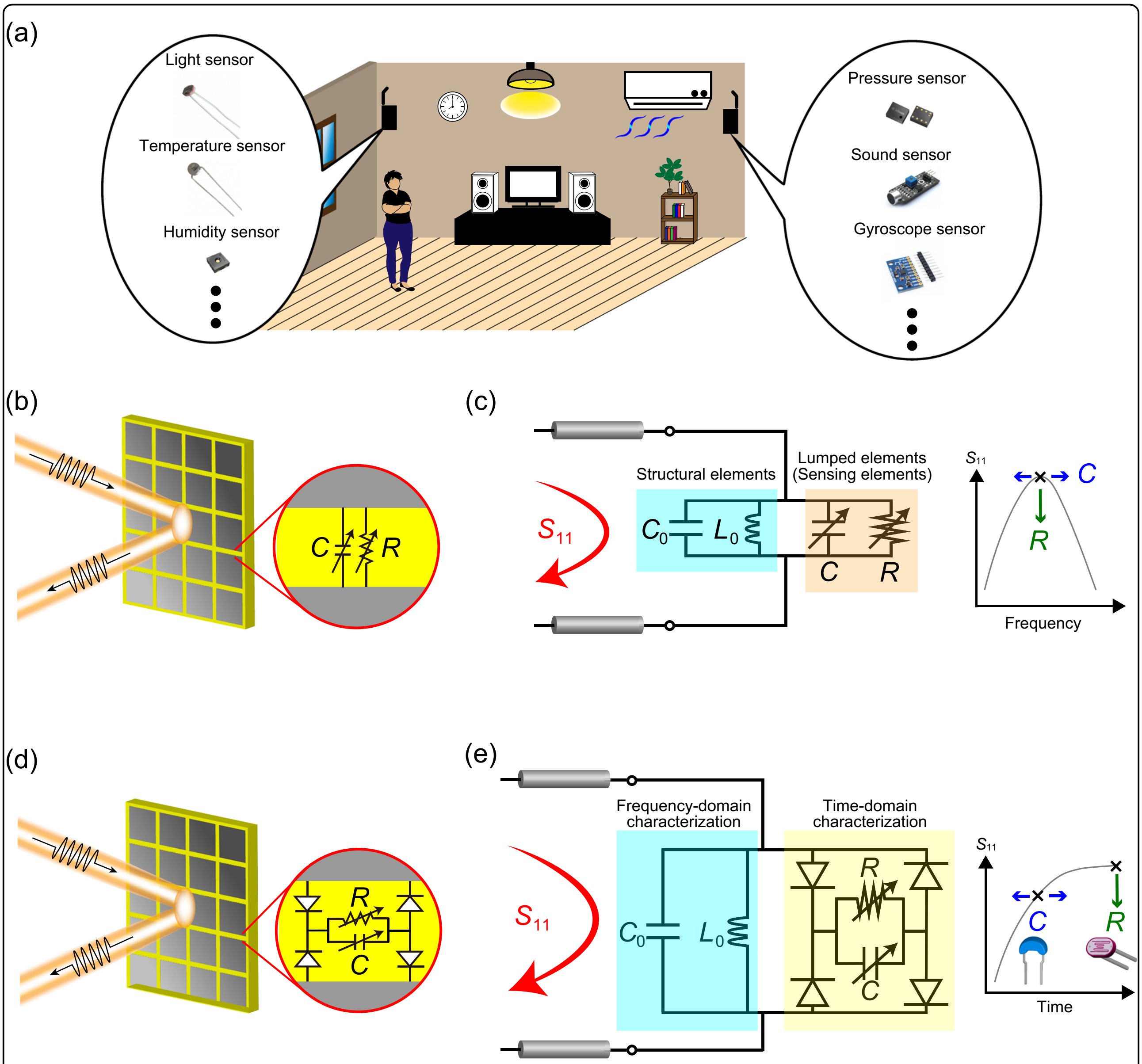

Fig. 1 Concept underlying the metasurface-based sensors. a Various sensors that are used in daily life. **b** Conventional metasurface-based sensor design using frequency-domain scattering profiles that address the issue of regular battery replacement and (**c**) a corresponding equivalent circuit model with scattering characteristics. Two circuit values (two physical properties) cannot be independently detected at a single frequency. **d** Proposed metasurface-based sensor design using time-domain scattering profiles that additionally address the restriction of limited frequency resources and (**e**) a corresponding equivalent circuit model with scattering characteristics. Even at the same frequency, two physical properties can be independently detected in the time domain by using diode bridges with sensing circuit elements such as photocells and temperature-dependent capacitors. This sensor design breaks harmonized oscillations and attains a large degree of freedom to detect multiple physical parameters.

metasurface unit cells (Fig. 1b)[14–18]. In this approach, every identified physical property is associated with a single resonant frequency. Thus, two physical properties can be identified via two independent resonant frequencies, which implies that two physical parameters cannot be independently detected at a single frequency (Fig. 1c). Moreover, in practice, the allocation of frequency resources is rigorously regulated[19–22]. Thus, the optimal scenario would include overcoming the frequency-domain restrictions imposed by classic resonant mechanisms and detecting multiple physical quantities at only a single frequency. For this reason, this study proposes metasurface-based sensors that change scattering profiles depending on the physical properties of the surrounding environment even at the same frequency (Fig. 1d, e). Our sensors are specifically designed to detect light intensity and temperature by integrating photocells and temperature-dependent capacitors. Importantly, however, these physical quantities are identified using only a single frequency because of time-domain scattering changes with a machine learning methodology[23,24]. By altering the integrated circuit layout, the design concept of our metasurface-based sensors may be extended to detect additional physical properties. Thus, this study helps achieve maintenance-free and sustainable next-generation wireless communication systems.

Results and discussion

Fundamental design theory

A key solution for detecting multiple physical quantities at the same frequency is to break the harmonized time-domain response. To this end, time-varying metasurfaces have been intensively studied and exploited for wavefront control, which aids in designing reconfigurable intelligent surfaces (RISs)[25–27], nonreciprocal wave propagation[28,29], and radiofrequency (RF) and optical devices[30,31]. Although most time-varying metasurfaces require external power sources such as active metasurfaces[26,32–34], passive and time-varying metasurfaces have been recently proposed to change the electromagnetic response even at the same frequency in accordance with the duration of the incoming pulse[31,35–37]; this approach is exploited in this study. In fact, these pulse-width-dependent metasurfaces, or so-called waveform-selective metasurfaces, rely on the well-known transients of classic direct current (DC) circuits. More specifically, waveform-selective metasurfaces comprise a periodic conducting pattern and resonate at resonant frequencies, as seen in ordinary metasurfaces[38,39]. However, by introducing a set of four diodes as a diode bridge into the gap between conductor edges, the waveform of the incoming wave (the sine function in this study) is fully rectified (as in the waveform based on |sin|), generating an infinite set of frequency components in which most of the energy is concentrated around the zero-frequency band. Therefore, transient phenomena can occur if the reactive circuit components are included inside the diode bridge. Specifically, this study uses a capacitor connected to a resistor in parallel inside the diode bridge. Under this circumstance, the reflection from the metasurface is reduced during an initial period because the incoming energy is stored in the capacitor and dissipated with the parallel resistor. However, by increasing the incident pulse width, the capacitor is fully charged so that the incident wave is poorly absorbed and strongly reflected even at the same frequency.

In particular, transient responses are characterized by time constants and steady-state resistance, which are associated with sensing circuit components whose circuit values vary in accordance with physical quantities. For example, some capacitors are well known to change their capacitance due to temperature changes. Additionally, photocells have variable resistance values in accordance with the surrounding light intensity. Therefore, by incorporating these circuit elements as parallel capacitors and resistors inside diode bridges, transients (or time-varying responses) change depending on the temperature and light intensity, which can be detected from scattering waves. Specifically, as explained in the literature[40] and the Supplementary Information (Supplementary Note 1), the time constant of our metasurface τ is determined by

$$\tau = \frac{CR_C R_d}{R_C + R_d}, \tag{1}$$

where C and R_C represent the capacitance and resistance, respectively, of the discrete components inside the diode bridge (i.e., the parallel capacitor and resistor). Additionally, R_d denotes the resistance of the two diodes at the turn-on voltage. In particular, if $R_C >> R_d$, τ is simplified to

$$\tau \sim CR_d, \tag{2}$$

which indicates that the transition time is mostly changed by C since the R_d is not adjustable. Additionally, in the steady state, the capacitor approaches an open circuit so that the reflecting state is related to the values of R_C and R_d. Thus, R_Cs can be exploited to control the steady-state response. Moreover, because C and R_C vary because of the temperature dependence of capacitors and the light-intensity dependence of photocells, our metasurface can detect temperature and light intensity in accordance with the reflected waveform. Note that although this study limits the multifunctional sensing capability to only two physical quantities, the proposed concept can be further extended to detect additional physical quantities by introducing extra circuit components. For example, the above capacitor-based circuit configuration can be integrated with an inductor-based circuit configuration to produce a reflectance peak, dip, or more advanced waveform, which can be associated with more than two circuit parameters in the time domain[41,42].

Numerical demonstration

Before experimental validation, we numerically show how metasurface-based sensors vary their time-domain response in accordance with circuit parameters. As shown in Fig. 2a, the unit cells of our metasurface comprise a ground plane, a dielectric substrate (Rogers 3003) and conducting patches with minor trimming to deploy small conducting pads and form a diode bridge including a parallel $R_C C$ circuit ($R_C = 10$ kΩ and $C = 1$ nF). For simplicity, these simulations use ordinary capacitors and resistors for C and R_C instead of a temperature-dependent

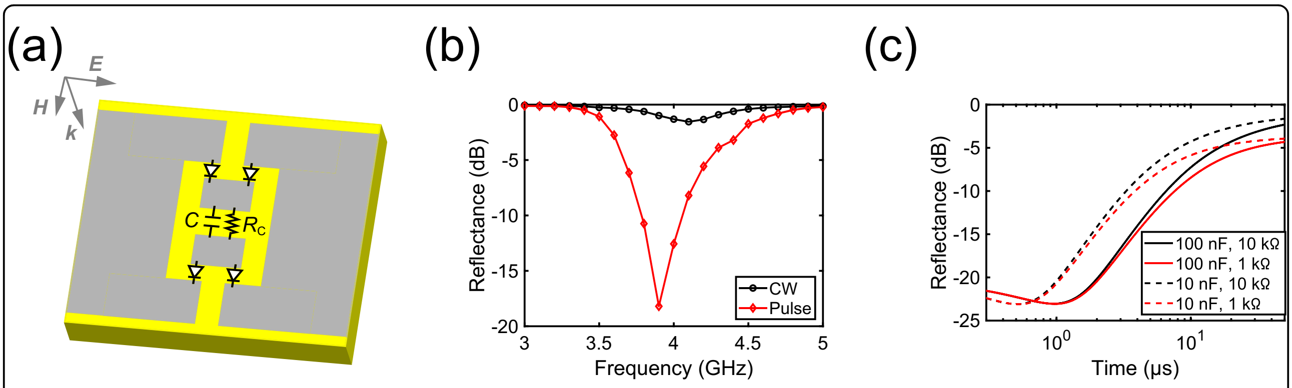

Fig. 2 Numerically simulated reflectance profiles. a Realistic unit cell model with periodic boundaries applied for the incident *E* and *H* directions. **b** Frequency-domain reflectance. *C*, R_C and the input power were set to 1 nF, 10 kΩ and 0 dBm, respectively. **c** Time-domain reflectance at 3.9 GHz with various *C* and R_C values.

capacitor and a photocell, respectively. Detailed information for these simulations is provided in the "Simulations" subsection of the Methods Section and the Supplementary Information (Supplementary Note 2), including the design parameters for the conducting geometry, substrate and lumped circuit elements. Under these circumstances, the reflecting profiles of the metasurface for 50-ns short pulses and continuous waves (CWs) varied, as shown in Fig. 2b. According to these simulation results, the metasurface considerably reduces the reflectance magnitude only for short pulses near 3.9 GHz, which is consistent with the pulse width-dependent absorbing mechanism explained earlier. To further clarify this reflectance trend, *C* and R_C were varied, as shown in Fig. 2c, which indicates that the transition time was shifted by increasing *C* from 10 nF to 100 nF. Additionally, the steady-state reflectance decreased with decreasing R_C from 10 kΩ to 1 kΩ. Importantly, these two conclusions also support the aforementioned theoretical design and ensure that two independent physical quantities can be detected if they are associated with changes in *C* and R_C. Related results and information are provided in the Supplementary Information (Supplementary Note 2).

Experimental demonstration

On the basis of the simulation results shown above, we fabricated and experimentally tested the metasurface-based sensor, as shown in Fig. 3a. For these measurements, our metasurface was composed of 15 × 15 unit cells and placed on a programmable hot plate that arbitrarily and directly controlled the temperature of the metasurface sample. Additionally, a light source was positioned in front of the metasurface and controlled by pulse width modulation (PWM) signals. In addition to these thermal and light sources, incident signals were radiated by a standard horn antenna, and another horn antenna was used to receive the reflected waveform. The incident and reflected angles were set to 30°, and the incident wave was a transverse electric (TE) polarized wave. Detailed information about the measurements is provided in the "Measurement Samples" and "Measurement Methods" subsections of the Methods Section and the Supplementary Information (Supplementary Note 2). Under these circumstances, the temperature of the metasurface and the surrounding light intensity were set to 22.1 °C and 328 lux, respectively, which provided nearly identical values of *C* and R_C as those shown in Fig. 2b (specifically, 10 nF and 10 kΩ). Thus, the frequency-domain profiles shown in Fig. 3b demonstrated a relatively low transmittance for short pulses near 3.76 GHz despite the use of the same frequencies, which was consistent with the simulation results in Fig. 2b. Note that the transmittance in Fig. 3b was entirely lower than that in Fig. 2b because the measurement was performed in open space to consider a realistic sensing environment, whereas the simulation was conducted with periodic boundaries as a simplified situation. Additionally, a minor frequency shift appeared in the measurements because of differences between the simulations and measurements, e.g., the incident angle and parasitic circuit parameters that only appeared in the measurement sample. However, despite these differences, the reflectance profile evidently varied in accordance with the incident waveform even during the measurements.

Next, we clarified how the time-domain response varied with changes in temperature and light intensity. In these measurements, we simplified the loaded circuits inside the diode bridges and used pairs of either temperature-dependent capacitors and fixed resistors or fixed capacitors and photocells, which facilitated the analysis of the temperature and light intensity dependences. First, pairs of temperature-dependent capacitors and fixed resistors (10 kΩ) were used with variable

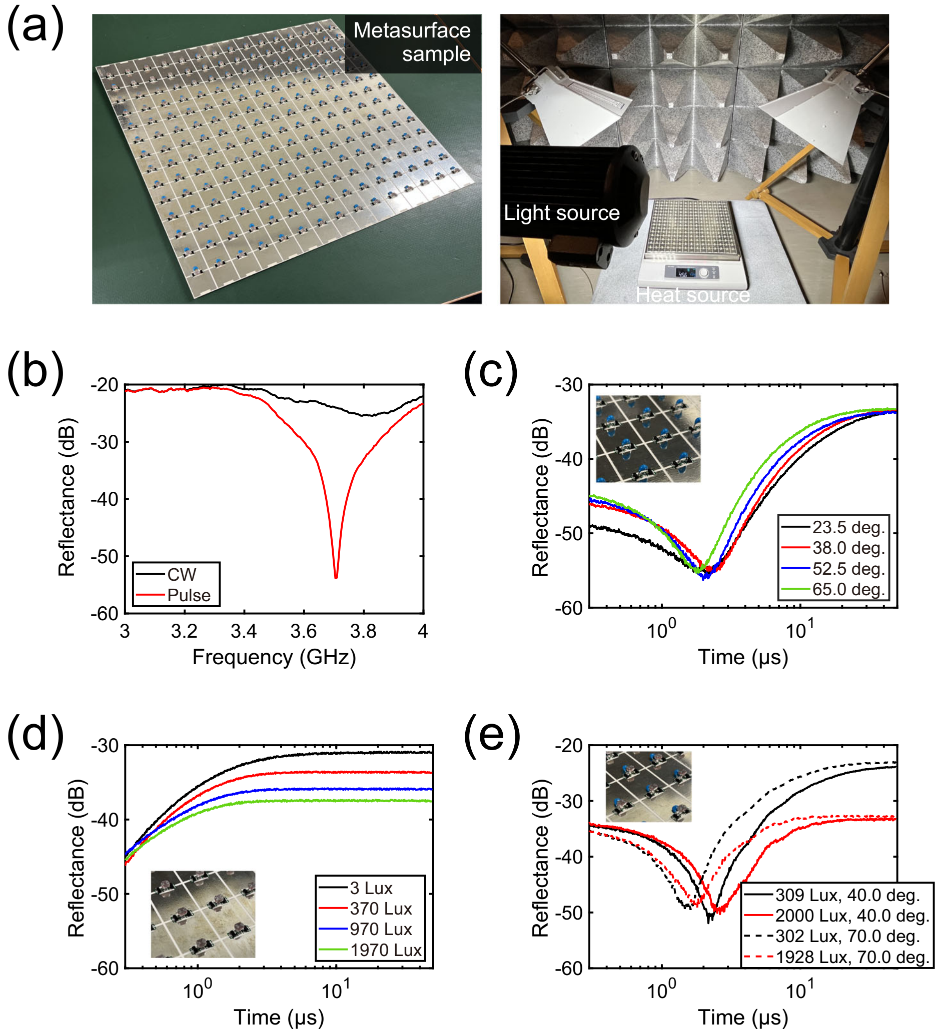

Fig. 3 Experimental validation. a Measurement sample and measurement system using light and heat sources in free space. **b** Frequency-domain reflectance. The temperature, light intensity and input power were set to 22.1 °C, 328 lux and 30 dBm, respectively. **c–e** Time-domain reflectance of the metasurface-based sensor using (**c**) temperature-dependent capacitors and fixed resistors (10 kΩ), (**d**) fixed capacitors (1 nF) and photocells and (**e**) temperature-dependent capacitors and photocells. The frequency was set to optimal values to increase the time-domain variation in (**c**–**e**) (specifically, 3.82 GHz in (**c**) and (**d**) and 3.76 GHz in (**e**)).

temperature values at 3.82 GHz, as shown in Fig. 3c. According to these measurements, the transition time decreased with increasing metasurface temperature from 23.5 °C to 65.0 °C because the capacitance of the temperature-dependent capacitors decreased, which decreased the time constant. This result was consistent with the numerical simulation in Fig. 2c and Eq. (2). Additionally, when pairs of fixed capacitors (1 nF) and photocells were alternatively used within the diode bridges, the metasurface varied the steady-state reflectance, as shown in Fig. 3d. Specifically, the reflectance decreased from −30.9 dB to −37.5 dB as the light intensity increased from 3 lux to 1970 lux, which resulted in a decrease in the effective resistive component of the photocells and strong absorption of the incident wave in the steady state.

Moreover, the metasurface was experimentally evaluated using the temperature-dependent capacitors and the photocells, as shown in Fig. 3e. This measurement result also ensures that the changes in temperature and light intensity affect the reflectance profiles. For example, by increasing the temperature from 40 to 70 °C, the time constant of the metasurface was reduced so that the reflectance curves were shifted to a smaller time scale (i.e., comparing the solid curves with the dashed curves). Additionally, increasing the light intensity from approximately 300 to 2000 lux decreased the steady-state reflectance from approximately −23 dB to −33 dB (see the

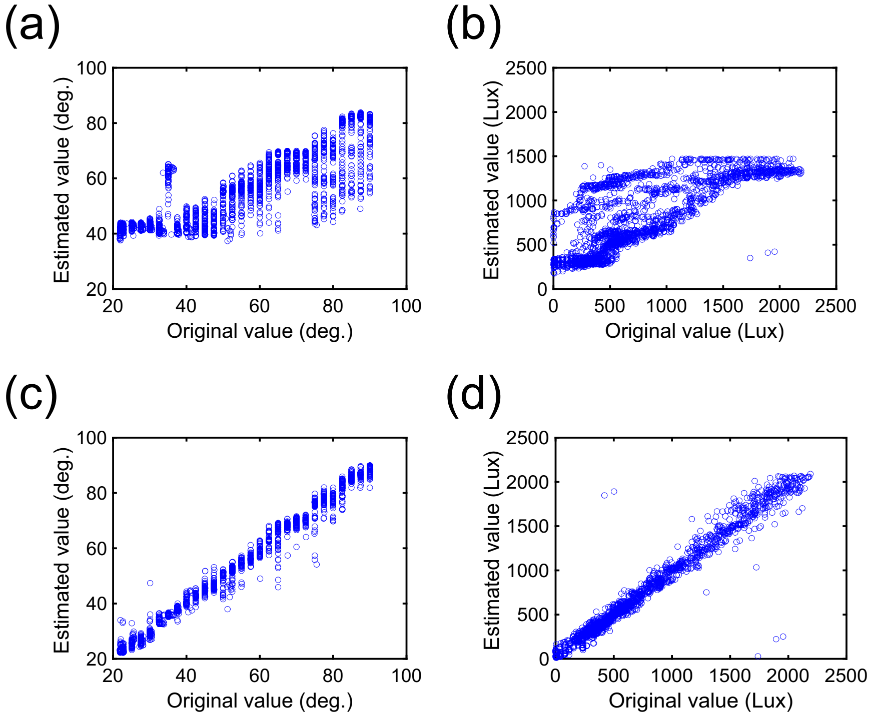

Fig. 4 Simultaneous estimation of temperature and light intensity from reflected waveforms. a, **b** Use of 11 training datasets for (**a**) temperature and (**b**) light intensity estimation. **c**, **d** Use of 458 training datasets for (**c**) temperature and (**d**) light intensity estimation. The determination coefficients of (**a**)–(**d**) were 0.6456, 0.5841, 0.9861 and 0.9610, respectively. Additional results are provided in the Supplementary Information (Supplementary Note 4).

difference between the black curves and the red curves). Therefore, by associating C and the R_C with physical quantities, our metasurface design independently controlled the time constant and the steady-state response. In the Supplementary Information (Supplementary Note 3), this metasurface-based approach is also demonstrated via simpler versions of structures such as microstrips and one-dimensional metasurface lines, which further validates the time-varying scattering effect even at the same frequency in accordance with the temperature and light intensity.

Estimation of physical quantities

We further present an approach to estimate temperature and light intensity on the basis of the physical quantities associated with C and R_C. Although other approaches are potentially applicable for predicting these two physical quantities (e.g., use of theoretical equivalent circuit models[40,43–45]), we adopted a machine learning approach based on random forest regression[24]. Our estimation approach was composed of four steps. First, the measured time-domain reflectance profiles were divided into 40 segments of time on a log scale. Second, in each segment, an average reflectance value was obtained. Third, these average reflectance values were used as explanatory variables for the training data. Finally, on the basis of the training data, the temperature and light intensity were estimated and compared to their actual values. We varied the number of training datasets and test datasets, while the total number of these datasets was fixed at 2290 (i.e., the ratio between the training datasets and test datasets was varied within the entire dataset of 2290). Further details are provided in the "Estimation Method" subsection of the Methods Section.

The corresponding estimation results are shown in Fig. 4. When only 11 datasets were used as training datasets in Fig. 4a, b, the correlation between the estimated values and the original values was poor, with determination coefficients of 0.6456 and 0.5841 for temperature and light intensity, respectively. However, by increasing the number of training datasets to 458, these determination coefficients improved to 0.9861 and 0.9610 for temperature and light intensity, respectively. These results indicate that a proper number of datasets need to be used for the training process, which is consistent with other reports on AI-based metasurface studies[46–48]. More importantly, these results validate that our metasurface-based sensors can be used to estimate physical quantities at the same frequency. The Supplementary Information (Supplementary Note 4) provides additional results, including the use of an estimation method other than random forest regression.

Discussion

Unlike conventional structures[11–13,38,49], our metasurfaces are passive yet able to break classic harmonic oscillations even at a fixed frequency owing to the lumped transient circuit elements, more specifically, their circuit values, such as capacitance and resistance. In particular, our metasurfaces enable us to control time-varying responses as the capacitance and resistance change depending on the surrounding environment, which has not been demonstrated in the literature[22,35–37,41]. Additionally, although our metasurface-based sensors behave differently in accordance with the pulse duration of the incident wave, as shown in Fig. 2b, the sensing process itself requires CWs (i.e., not different pulses), as shown in Fig. 2c. Therefore, our metasurface-based sensors do not need additional complicated modulation techniques if the pulse width is sufficiently long. In the literature, waveform-selective metasurfaces are integrated with an antenna design to tailor antenna characteristics, including radiation patterns in accordance with the pulse duration even at a constant frequency[22,50,51]. To date, the concept of such waveform selectivity has been introduced into, for instance, sensors[22], RISs[27,52], IoT tags[53] and signal processing[31,54]. However, unlike conventional studies, our metasurfaces allow us to control time-varying responses via changes in the circuit values of lumped components, as mentioned above. Note that our machine learning approach itself is quite ordinary and readily available from, for instance, the built-in functions of Python. This machine learning approach cannot predict physical quantities without our metasurfaces, which indicates that the uniqueness of our study lies in our metasurface design but not in the machine learning approach.

Our metasurface-based sensing approach was experimentally validated to be capable of estimating more than one physical quantity by breaking the harmonic oscillation of metasurfaces in the time domain and using only one frequency component. Our approach is rational because the use of frequency resources is strictly determined in practice to avoid electromagnetic interference issues[19–21]. This approach may apply to one of the industrial, scientific and medical (ISM) bands, where frequency resources are readily available without rigorous license issues for the use of radio-frequency (RF) waves. Moreover, our approach is useful for managing and designing future IoT systems. Conventionally, IoT sensors were designed to obtain multidimensional and multimodal information for realizing next-generation IoT systems, including cyber-physical space, digital twins, autonomous driving, smart cities and VR/AR[1,2,5]. However, this conventional approach requires regular replacement of internal batteries to maintain communication with external internet/cloud systems. Because the number of IoT sensors is increasing rapidly, maintaining all IoT sensors manually and replacing their batteries will soon be unrealistic. Here, our metasurface-based approach does not require the use of batteries but permits the sensing of multiple physical quantities, addressing an emerging issue in the design of future IoT systems. In particular, although this study was limited to sensing two physical quantities as a proof of concept, our approach can be extended to sensing more than two physical quantities by adding additional circuit components that react with other physical quantities and characterize the time-domain response of metasurfaces[37,41,42].

For more practical use as IoT sensors, further improvements of our metasurface-based sensors are required. For example, the metasurfaces demonstrated in this study rely on commercial diodes that require a large amount of input power to rectify incoming signals and vary the time-domain response associated with physical quantities. Therefore, reducing the power level by using customized low-power diodes helps design battery-free metasurface-based multifunctional sensors in an energy-efficient manner. Additionally, the successful implementation of our approach in realistic environments depends on how reflected (or scattered) waveforms are associated with physical quantities. This study addressed this issue by exploiting random forest regression, which provided excellent determination coefficients larger than 0.96. Although other sensor technologies may provide greater accuracy, our determination coefficient can be further improved by adopting other machine learning techniques suited for individual application scenarios (refer to Supplementary Note 4 in the Supplementary Information). Moreover, cost-effectiveness is an important point in our study since the proposed metasurface-based sensors are maintenance-free and do not require human resources to replace the batteries of conventional IoT sensors. Therefore, the proposed approach only requires the fabrication cost of the metasurfaces. This cost-effectiveness can be further evaluated and discussed in future studies. The present study evaluated our metasurfaces with plane waves but not with spatially modulated waves[55–57], which can be exploited as an additional degree of freedom to sense physical quantities. At the same time, however, the use of spatial modulation may narrow the applicable sensing scenarios in terms of the angles of the incident wave and the metasurface. Finally, connecting our sensing approach to IoT/cloud systems is an important issue that is not fully demonstrated in this study. In particular, real-time feedback is needed for IoT systems in cyber-physical space, smart cities, autonomous driving, farming and health care[58–61], where wireless networks are expected to reduce the estimation time for physical quantities by using, for example, simplified learning models and fast-speed calculation approaches.

Conclusion

In conclusion, we present a metasurface-based sensor design that achieves multifunctional sensing without the need for multiple frequencies or an external power supply. Our metasurface showed variable reflectance profiles in the time domain, which were independently determined by lumped circuit parameters that were responsive to the two physical quantities of interest, specifically, temperature and light intensity. Additionally, we introduced an approach to estimate the temperature and light intensity from the reflected waveform of the metasurface via random forest regression. Thus, the temperature and light intensity were successfully detected, with determination coefficients of 0.9861 and 0.9610, respectively. Our study affords new possibilities for sensing multiple physical quantities without the need for an external power supply or several frequencies, which facilitates the design of next-generation wireless communication systems.

Methods

Simulations

Numerical simulations were performed via a cosimulation method in ANSYS Electronics Desktop (version R2) 2022. This method models metasurfaces in an electromagnetic solver (HFSS). Importantly, all of the discrete circuit components were replaced with lumped ports. The scattering parameters of the metasurfaces were then used in a circuit simulator (Circuit) as circuit models. In these circuit simulations, lumped ports were connected to the actual circuit components used, which was equivalent to directly including the circuit components in electromagnetic simulations. However, this cosimulation method facilitated the entire simulation process for readily obtaining the final simulation results compared with stand-alone electromagnetic simulation approaches[62]. Short-pulse simulations (as shown by the red curve in Fig. 2b) were conducted via 50-ns pulses. In this case, the total reflected energy was compared with the total incident energy to calculate the reflectance. Additionally, CW simulations (as shown by the black curve in Fig. 2b) were performed via the harmonic balance approach, where the steady-state response was directly obtained. Here, we calculated the reflectance by dividing the reflected energy by the incident energy during 2 cycles. Moreover, we also calculated the transient reflectance in the time domain (as shown in Fig. 2c). In this case, the time-varying reflectance was obtained by calculating the moving average of the reflected energy for 250 ns with discretized 100 ps time steps and comparing it with the moving average of the incident energy. The detailed design parameters of the simulation models are given in the Supplementary Information (Supplementary Note 2).

Measurement samples

Our metasurface measurement samples consisted of a ground plane, a dielectric substrate (Rogers 3003) and a periodic array of square conducting patches with minor trimming to connect discrete circuit components. These design parameters are fully summarized in the Supplementary Information (Supplementary Note 2). The diodes used were provided by Avago (HSMS-286x series). The temperature-dependent capacitors and photocells were produced by Murata Manufacturing Co. (RDEF51H013Z0P1H03B) and Luna Innovations (NSL-19M51), respectively.

Measurement method

Although detailed measurement setups are illustrated in the Supplementary Information (Supplementary Note 2), to characterize frequency-domain profiles (as shown in Fig. 3b), we used not only a vector network analyzer (VNA) (Keysight Technologies, N5249A) but also an amplifier (Ophir, 5193RF) to sufficiently increase the input power level and turn on the diodes loaded on the metasurfaces. For time-domain profiles (e.g., those shown in Fig. 3c to Fig. 3e), we used a signal generator (Anritsu, MG3692C) as a signal source. Similarly, the abovementioned amplifier was used to ensure that the input power level was sufficiently large. Additionally, an isolator was used to protect the amplifier and the signal generator from excessive reflection. Part of the incident wave was sent to an oscilloscope (Keysight, DSOX6002A), while most of the energy was radiated to the metasurfaces through a standard horn antenna (Schwarzbeck Mess-Elektronik, BBHA9120D). Importantly, the surrounding light intensity and the temperature of the metasurfaces were controlled by a light source (Safego, C36W-FL) and a programmable hot plate (AS ONE, ND-2A). These light and heat sources were arbitrarily controlled by pulse width modulation (PWM) and proportional–integral–derivative (PID) control, respectively. Owing to these two sources, the metasurfaces varied the reflected waveforms that were received by another horn antenna and measured by the oscilloscope. As mentioned in the above “Simulations” subsection, the transient reflectance varying in the time domain was obtained by comparing the reflected energy with the incident energy.

Estimation methods

The reflected waveform was used to estimate the actual temperature and light intensity. This study used Python program codes based on random forest regression to obtain the results shown in Fig. 4. Here, we used a built-in function of Phyton (specifically, "split") to select training datasets at random from all of the measurement datasets (2290 in total), while the remaining datasets were used as test datasets. For example, in Fig. 4a, b, 11 datasets were selected at random as training datasets, whereas the remaining 2279 datasets (=2290 to −11) were used as test datasets. In Fig. 4c, d, the number of training datasets was increased to 458, whereas that of the test datasets was reduced to 1832. In the Supplementary Information (Supplementary Note 4), the relationship between the number of training datasets and the number of test datasets was varied to demonstrate how these numbers influence the estimation performance. Ridge regression[63] was also alternatively applied to estimate the temperature and light intensity in the Supplementary Information (Supplementary Note 4).

Acknowledgements

This work was supported in part by the Japan Science and Technology Agency (JST) under Fusion Oriented Research for Disruptive Science and Technology (FOREST) and under Precursory Research for Embryonic Science and Technology (PRESTO) Nos. JPMJPR193A, JPMJPR1932 and JPMJPR2134 and the National Institute of Information and Communications Technology (NICT), Japan, under commissioned research No. 06201.

Author details

[1]Department of Engineering, Nagoya Institute of Technology, Nagoya, Aichi 466-8555, Japan. [2]Precursory Research for Embryonic Science and Technology (PRESTO), Japan Science and Technology Agency (JST), Kawaguchi, Saitama 332-0012, Japan. [3]Research Center for Materials Nanoarchitechonics (MANA), National Institute for Materials Science (NIMS), Tsukuba, Ibaraki 305-0044, Japan. [4]Faculty of Pure and Applied Physics, University of Tsukuba, Tsukuba, Ibaraki 305-8577, Japan. [5]Graduate School of Science and Technology, Keio University, Yokohama, Kanagawa 223-8522, Japan. [6]Graduate School of Information Science and Technology, Osaka University, Suita, Osaka 565-0871, Japan

Author contributions

H.W. conceived the concept of the project. M.T., K.I., and K.A. conducted the simulations and measurements and analyzed the results. H.W., S.I., Y.S., and A.U. supervised these simulations and measurements and supported their data analysis. H.W. wrote the manuscript, and all the authors commented on it.

Data availability

The data that support the findings of this study are available from the corresponding author upon request.

Competing interests

The authors declare no competing interests.

Publisher's note

Supplementary information The online version contains supplementary material available at https://doi.org/10.1038/s41427-024-00574-4.

Received: 7 June 2024 Revised: 25 August 2024 Accepted: 4 September 2024

References

1. Gubbi, J., Buyya, R., Marusic, S. & Palaniswami, M. Internet of things (IoT): a vision, architectural elements, and future directions. *Futur. Gener. Comput. Syst.* **29**, 1645–1660 (2013).
2. Al-Fuqaha, A., Guizani, M., Mohammadi, M., Aledhari, M. & Ayyash, M. Internet of things: a survey on enabling technologies, protocols, and applications. *IEEE Commun. Surv. Tutor.* **17**, 2347–2376 (2015).
3. Dang, S., Amin, O., Shihada, B. & Alouini, M.-S. What should 6G be? *Nat. Electron.* **3**, 20–29 (2020).
4. Wilson, J. S. *Sensor Technology Handbook* (Elsevier, 2004).
5. Tao, F., Zhang, H., Liu, A. & Nee, A. Y. C. Digital twin in industry: state-of-the-art. *IEEE Trans. Ind. Inform.* **15**, 2405–2415 (2018).
6. Liu, N., Mesch, M., Weiss, T., Hentschel, M. & Giessen, H. Infrared perfect absorber and its application as plasmonic sensor. *Nano Lett.* **10**, 2342–2348 (2010).
7. Schueler, M., Mandel, C., Puentes, M. & Jakoby, R. Metamaterial inspired microwave sensors. *IEEE Microw. Mag.* **13**, 57–68 (2012).
8. Ebrahimi, A., Withayachumnankul, W., Al-Sarawi, S. & Abbott, D. High-sensitivity metamaterial-inspired sensor for microfluidic dielectric characterization. *IEEE Sens. J.* **14**, 1345–1351 (2013).
9. Sreekanth, K. V. et al. Extreme sensitivity biosensing platform based on hyperbolic metamaterials. *Nat. Mater.* **15**, 621–627 (2016).
10. Hu, X. et al. Metamaterial absorber integrated microfluidic terahertz sensors. *Laser Photonics Rev.* **10**, 962–969 (2016).
11. Yu, N. et al. Light propagation with phase discontinuities: generalized laws of reflection and refraction. *Science* **334**, 333–337 (2011).
12. Pfeiffer, C. & Grbic, A. Metamaterial Huygens' surfaces: tailoring wave fronts with reflectionless sheets. *Phys. Rev. Lett.* **110**, 197401 (2013).
13. Yu, N. & Capasso, F. Flat optics with designer metasurfaces. *Nat. Mater.* **13**, 139–150 (2014).
14. Driscoll, T. et al. Memory metamaterials. *Science* **325**, 1518–1521 (2009).
15. Liu, M. et al. Terahertz-field-induced insulator-to-metal transition in vanadium dioxide metamaterial. *Nature* **487**, 345–348 (2012).
16. Tao, H. et al. Reconfigurable terahertz metamaterials. *Phys. Rev. Lett.* **103**, 147401 (2009).
17. Ren, Z. et al. Leveraging of MEMS technologies for optical metamaterials applications. *Adv. Opt. Mater.* **8**, 1900653 (2020).
18. Lin, W. & Ziolkowski, R. W. Wirelessly powered light and temperature sensors facilitated by electrically small omnidirectional and Huygens dipole antennas. *Sensors* **19**, 1998 (2019).
19. The European table of frequency allocations and applications in the frequency range 8.3 khz to 3000 ghz (eca table) Approved November 2020 (2020).
20. *FCC* online table of frequency allocations 47 c.f.r. §2.106. Revised on February 1, 2021. (2021)
21. MIC: The Radio Use Web Site. MIC Frequency Assignment Plan, September 2021. https://www.tele.soumu.go.jp/e/adm/freq/search/share/plan.htm (2021).
22. Ushikoshi, D. et al. Pulse-driven self-reconfigurable meta-antennas. *Nat. Commun.* **14**, 633 (2023).
23. Tibshirani, R. Regression shrinkage and selection via the Lasso. *J. R. Stat. Soc. Ser. B: Stat. Methodol.* **58**, 267–288 (1996).
24. Breiman, L. Random forests. *Mach. Learn.* **45**, 5–32 (2001).
25. Wu, Q. & Zhang, R. Towards smart and reconfigurable environment: intelligent reflecting surface aided wireless network. *IEEE Commun. Mag.* **58**, 106–112 (2020).
26. Zhang, L. et al. Space-time-coding digital metasurfaces. *Nat. Commun.* **9**, 4334 (2018).
27. Fathnan, A. A. et al. Unsynchronized reconfigurable intelligent surfaces with pulse-width-based design. *IEEE Trans. Veh. Technol.* **72**, 15103–15108 (2023).
28. Caloz, C. et al. Electromagnetic nonreciprocity. *Phys. Rev. Appl.* **10**, 047001 (2018).
29. Nagulu, A., Reiskarimian, N. & Krishnaswamy, H. Non-reciprocal electronics based on temporal modulation. *Nat. Electron.* **3**, 241–250 (2020).
30. Barbuto, M. et al. Metasurfaces 3.0: a new paradigm for enabling smart electromagnetic environments. *IEEE Trans. Antennas Propag.* **70**, 8883–8897 (2022).
31. Takimoto, K. et al. Perfect pulse filtering under simultaneous incidence at the same frequencies with waveform-selective metasurfaces. *APL Mater.* **11**, 081116 (2023).
32. Liu, M., Powell, D. A., Zarate, Y. & Shadrivov, I. V. Huygens' metadevices for parametric waves. *Phys. Rev. X.* **8**, 031077 (2018).

33. Taravati, S. & Eleftheriades, G. V. Full-duplex reflective beamsteering metasurface featuring magnetless nonreciprocal amplification. *Nat. Commun.* **12**, 4414 (2021).
34. Moussa, H. et al. Observation of temporal reflection and broadband frequency translation at photonic time interfaces. *Nat. Phys.* **19**, 863–868 (2023).
35. Wakatsuchi, H., Kim, S., Rushton, J. J. & Sievenpiper, D. F. Waveform-dependent absorbing metasurfaces. *Phys. Rev. Lett.* **111**, 245501 (2013).
36. Wakatsuchi, H., Long, J. & Sievenpiper, D. F. Waveform selective surfaces. *Adv. Funct. Mater.* **29**, 1806386 (2019).
37. Takeshita, H. et al. Frequency-hopping wave engineering with metasurfaces. *Nat. Commun.* **15**, 196 (2024).
38. Sievenpiper, D., Zhang, L., Broas, R. F. J., Alexopolous, N. G. & Yablonovitch, E. High-impedance electromagnetic surfaces with a forbidden frequency band. *IEEE Trans. Microw. Theory* **47**, 2059–2074 (1999).
39. Munk, B. A. *Frequency Selective Surfaces: Theory and Design* (John Wiley & Sons, 2005). https://doi.org/10.1002/0471723770.
40. Asano, K., Nakasha, T. & Wakatsuchi, H. Simplified equivalent circuit approach for designing time-domain responses of waveform-selective metasurfaces. *Appl. Phys. Lett.* **116**, 171603 (2020).
41. Wakatsuchi, H. et al. Waveform selectivity at the same frequency. *Sci. Rep.* **5**, 9639 (2015).
42. Wakatsuchi, H. Time-domain filtering of metasurfaces. *Sci. Rep.* **5**, 16737 (2015).
43. Baena, J. D. et al. Equivalent-circuit models for split-ring resonators and complementary split-ring resonators coupled to planar transmission lines. *IEEE Trans. Microw. Theory Tech.* **53**, 1451–1461 (2005).
44. Zhou, L., Liu, L. & Shen, Z. High-performance energy selective surface based on the double-resonance concept. *IEEE Trans. Antennas Propag.* **69**, 7658–7666 (2021).
45. Bakshi, S. C., Mitra, D. & Teixeira, F. L. Wide-angle broadband rasorber for switchable and conformal application. *IEEE Trans. Microw. Theory* **69**, 1205–1216 (2021).
46. Qian, C. et al. Deep-learning-enabled self-adaptive microwave cloak without human intervention. *Nat. Photonics* **14**, 383–390 (2020).
47. Wen, E., Yang, X. & Sievenpiper, D. F. Real-time 2-D beamforming with rotatable dielectric slabs enabled by generative neural network. *IEEE Trans. Antennas Propag.* **70**, 8360–8367 (2022).
48. Liu, C. et al. A programmable diffractive deep neural network based on a digital-coding metasurface array. *Nat. Electron* **5**, 113–122 (2022).
49. Tsiftsis, T. A., Valagiannopoulos, C., Liu, H., Boulogeorgos, A.-A. A. & Miridakis, N. I. Metasurface-coated devices: a new paradigm for energy-efficient and secure 6G communications. *IEEE Veh. Technol. Mag.* **17**, 27–36 (2022).
50. Vellucci, S., Monti, A., Barbuto, M., Toscano, A. & Bilotti, F. Waveform-selective mantle cloaks for intelligent antennas. *IEEE Trans. Antennas Propag.* **68**, 1717–1725 (2020).
51. Barbuto, M. et al. Waveguide components and aperture antennas with frequency- and time-domain selectivity properties. *IEEE Trans. Antennas Propag.* **68**, 7196–7201 (2020).
52. Fathnan, A. A., Homma, H., Sugiura, S. & Wakatsuchi, H. Method for extracting the equivalent admittance from time-varying metasurfaces and its application to self-tuned spatiotemporal wave manipulation. *J. Phys. D: Appl. Phys.* **56**, 015304 (2023).
53. Tashiro, M., Fathnan, A. A., Sugiura, Y., Uchiyama, A. & Wakatsuchi, H. Metasurface-inspired maintenance-free Internet of things tags characterised in both frequency and time domains. *Electron. Lett.* **58**, 937–939 (2022).
54. Imani, M. F. & Smith, D. R. Temporal microwave ghost imaging using a reconfigurable disordered cavity. *Appl. Phys. Lett.* **116**, 054102 (2020).
55. Cui, T. J., Qi, M. Q., Wan, X., Zhao, J. & Cheng, Q. Coding metamaterials, digital metamaterials and programmable metamaterials. *Light Sci. Appl.* **3**, e218–e218 (2014).
56. Tsilipakos, O., Koschny, T. & Soukoulis, C. M. Antimatched electromagnetic metasurfaces for broadband arbitrary phase manipulation in reflection. *ACS Photonics* **5**, 1101–1107 (2018).
57. Valagiannopoulos, C., Tsiftsis, T. A. & Kovanis, V. Metasurface-enabled interference mitigation in visible light communication architectures. *J. Opt.* **21**, 115702 (2019).
58. Celesti, A. et al. An IoT cloud system for traffic monitoring and vehicular accidents prevention based on mobile sensor data processing. *IEEE Sens. J.* **18**, 4795–4802 (2018).
59. Plageras, A. P., Psannis, K. E., Stergiou, C., Wang, H. & Gupta, B. B. Efficient IoT-based sensor BIG Data collection–processing and analysis in smart buildings. *Futur. Gener. Comput. Syst.* **82**, 349–357 (2018).
60. Sood, K. et al. Accurate detection of IoT sensor behaviors in legitimate, faulty and compromised scenarios. *IEEE Trans. Dependable Secur. Comput.* **20**, 288–300 (2023).
61. Harb, H., Mansour, A., Nasser, A., Cruz, E. M. & de la Torre Díez, I. A sensor-based data analytics for patient monitoring in connected healthcare applications. *IEEE Sens. J.* **21**, 974–984 (2021).
62. Wakatsuchi, H., Anzai, D. & Smartt, C. Visualization of field distributions of waveform-selective metasurface. *IEEE Antennas Wirel. Propag. Lett.* **15**, 690–693 (2016).
63. Hoerl, A. E. & Kennard, R. W. Ridge regression: biased estimation for nonorthogonal problems. *Technometrics* **42**, 80 (2000).